TRENDS IN SCIENCES 2026; 23(12): 14859
https://doi.org/10.48048/tis.2026.14859 RESEARCH ARTICLE

Morphological Control of Cobalt Ferrite Using Ionic Liquids for Enhanced Optical and Electrocatalytic Properties

Md Hasibul Hasan[1,2] and Md. Abu Bin Hasan Susan[1,*]

[1]*Department of Chemistry, University of Dhaka, Dhaka 1000, Bangladesh*
[2]*Department of Chemistry, Virginia Tech, Blacksburg, Virginia 24060, United States*

([*]Corresponding author's e-mail: susan@du.ac.bd)

Received: 23 March 2026, Revised: 31 May 2026, Accepted: 30 June 2026, Published: 1 July 2026

Abstract

The morphology of cobalt ferrite ($CoFe_2O_4$) plays a crucial role in governing optoelectronic and catalytic properties by influencing electron transport and surface reactivity. In this work, $CoFe_2O_4$ was synthesized with varying morphology using an ionic liquid (IL)-assisted hydrothermal method from iron(III) nitrate nonahydrate and cobalt(II) nitrate hexahydrate. Two ILs, 1-ethyl-3-methylimidazolium trifluoromethanesulfonate ($[C_2mim]CF_3SO_3$) and 1-ethyl-3-methylimidazolium methanesulfonate ($[C_2mim]CH_3SO_3$), which share a common cation but differ in physicochemical properties, were used as soft templates to tailor morphology. Formation of $CoFe_2O_4$ and removal of IL were confirmed using Fourier transform infrared (FTIR) and energy-dispersive X-ray (EDX) spectroscopic techniques. IL modified the particle shape from a nanocube to a nanosphere and played a decisive role in controlling particle size through growth modifications. Five times smaller particles (17 nm) compared to native $CoFe_2O_4$ (84 nm) were obtained using ILs. A narrower size distribution, with smaller hydrodynamic diameters, was observed for ILs, as shown by dynamic light scattering (DLS) analysis. Highly crystalline, pure face-centered cubic (FCC) spinel structures were obtained using $[C_2mim]CH_3SO_3$. The optical band gap energy of $CoFe_2O_4$ was reduced from 1.93 to 1.83 eV in the presence of $[C_2mim]CH_3SO_3$ due to changes in cationic distribution and charge transfer induced by the IL. A low onset overpotential of 303 mV in 1.0 M KOH was observed in $CoFe_2O_4$ synthesized using $[C_2mim]CH_3SO_3$, indicating enhancement of electrocatalytic properties due to a higher number of active sites, smaller particles, and exposed facets. However, the lowest Tafel slope of 103 mV dec^{-1} was obtained for $[C_2mim]CF_3SO_3$ due to the faster kinetics on the electronically modified surface induced by fluorine-based anion. In IL-assisted $CoFe_2O_4$, the predominant (111) facet and modified surface structure might be responsible for improved performance in the oxygen evolution reaction (OER). This study demonstrates the tunability of optical and electrocatalytic properties of $CoFe_2O_4$ by controlling growth and formation of NPs using ILs.

Keywords: Cobalt ferrite, Ionic liquid, Soft templates, Morphology, Optical properties, Electrocatalysis, Oxygen evolution reaction

Introduction

The production of green hydrogen via electrochemical water splitting (WS) has gained significant attention due to the current emphasis on decarbonization and the production of energy from renewable sources [1,2]. Among the 2 half-reactions of WS, the oxygen evolution reaction (OER) is sluggish due to its four-electron transfer pathway. Thus, formation of the O−O bond requires a substantial amount of overpotential beyond the thermodynamic potential of 1.23 V under alkaline conditions [3]. Noble metal oxides are frequently employed as efficient catalysts to boost the reaction kinetics [4]. However, their limited availability and high cost prevent the wide-scale applications. Efforts are being made to find efficient catalysts from earth-abundant materials that

have high activity for the OER. Magnetic nanoparticles (NPs), such as spinel cobalt ferrite ($CoFe_2O_4$), are gaining substantial attention as a promising OER catalyst because of their redox versatility, improved catalytic activity, and stability originating from the mixed metal (Fe-Co) occupancies and stable crystal structure [5,7]. Beyond electrocatalysis, $CoFe_2O_4$ is a robust semiconductor that enables the harvesting of visible light for photocatalysis and optoelectronic applications [8,9]. Both optical properties and electrocatalytic performance of $CoFe_2O_4$ are dependent on morphology and cationic distribution between octahedral and tetrahedral sites [10,11].

Nano $CoFe_2O_4$ demonstrates distinct properties originating from the morphology and quantum size effect [12,13]. Morphological tunability makes it a promising catalyst, in which facets, shape, and electromagnetic properties strongly influence the process [14,17]. Therefore, OER performance of $CoFe_2O_4$ can be tuned by modifying crystal structure to obtain desired morphology, cationic distribution, and active facet for OER. Cooperative interaction between octahedral Co and tetrahedral Fe can lower the overpotential by 200 mV, as shown by the first-principles analysis at (100) and (001) facets [18]. $CoFe_2O_4$ is intrinsically more OER active on the (111) facet over the (001) facet because of the favorable OH^- adsorption [19]. Density functional theory (DFT) demonstrates that Fe^{3+} enrichment on the octahedral site reduces the free energy of OH* and OOH* intermediates in the (001) facet [18]. Morphology can impact the OER performance by enriching the (111) facet. Along with this, controlling the cationic distribution between octahedral (A) and tetrahedral (B) sites modifies the spin polarization, which in turn tunes the electrocatalytic activities. On the other hand, the optical band gap of $CoFe_2O_4$ also varies with morphology and local cationic distribution [20]. The optical properties of $CoFe_2O_4$ are governed by the *d-d* transition, charge transfer transition, and O (2p) to Fe/Co (3d) transition. The degree of inversion (occupancies of Co^{2+} on the octahedral site) influences the band gap, which indicates cationic-site-dependent optical properties [21]. The optical band gap is reduced from 1.9 to 1.7 eV with increasing particle size, suggesting the quantum size effect in optical properties [22].

The methods of synthesis highly influence the optical and catalytic properties of $CoFe_2O_4$ at the nanoscale. Numerous efforts have been made to control morphology and cationic distribution via an innovative methodology of synthesis. Mesoporous $CoFe_2O_4$ nanospheres with a size range of 120 to 180 nm were synthesized by Reddy *et al.* [23] utilizing a hydrothermal method. Phase-pure $CoFe_2O_4$ NPs with ultrasmall size ranging from 9.4 to 28.0 nm were synthesized by adjusting the reaction time from 6 to 24 h [24]. However, hydrothermal reaction alone has lower controllability to achieve the desired morphology with phase purity. A template-based synthesis allows precise control over the shape and size of $CoFe_2O_4$ NPs. Refat *et al.* [25] studied growth behavior of spherical $CoFe_2O_4$ NPs in a hydrothermal process with tuning reaction parameters and quantity of Arabic gum to modulate the optical band gap energy within the range of 1.6 to 1.9 eV. Impurity-free $CoFe_2O_4$ nano-octahedral grains, approximately 20 nm in size, were synthesized by Lopes-Moriyama *et al.* [26] using a hydrothermal method by adjusting reaction time, temperature, precursor concentration, and pH in the presence of cetyltrimethylammonium bromide (CTAB). Ji *et al.* [27] prepared pure $CoFe_2O_4$ nanorods having a diameter of 25 nm and lengths of up to 120 nm using CTAB-assisted anisotropic growth along (100). Ansari *et al.* [20] produced $CoFe_2O_4$ NPs with controllable particle size, shape, and chemical composition using different concentrations of oleic acid (OA) in a hydrothermal method. By altering the OA concentration, they achieved cubic, crystalline, chemically uniform, and nanoscale (5 to 15 nm) $CoFe_2O_4$ [20]. Huang *et al.* [28] synthesized ordered mesoporous $CoFe_2O_4$ utilizing the Santa Barbara Amorphous (SBA)-15, which exhibits a low overpotential (342 mV) to obtain 10 mA cm^{-2} in OER with a Tafel slope of 57.1 mV dec^{-1} [18]. Nano $CoFe_2O_4$ having a 20 nm size can achieve an ultralow onset overpotential of 260 mV and a low Tafel slope of 44 mV dec^{-1} [28]. These results showcase the template-assisted morphological tunability of $CoFe_2O_4$ for optical and electrocatalytic properties. Alternatives are necessary, nevertheless, given the challenges of eliminating templates and their negative impact on the NPs.

Ionic liquids (ILs), which consist of a bulky cation and an anion, are considered soft templates to produce

controlled nanostructures. Their designable physicochemical properties (viscosity, surface tension, hydrogen-bond donor/acceptor) can be systematically tuned by changing cation and anion, which enables precise control of nucleation and growth rate. ILs control growth and nucleation by van der Waals forces, hydrogen bonding, π-π stacking, and other supramolecular interactions [29]. However, understanding the growth and nucleation behavior of $CoFe_2O_4$ using IL is still in the rudimentary stage. Only 2 have been reported; among them, Ghaemi *et al.* [30] employed octyl-4-aza-1-azoniabicyclo[2.2.2]octane bromide ([C_8dabco]Br) to produce nanosheets, nanorods, and pastel-like morphology of $CoFe_2O_4$ by altering the (IL: Fe: Co) ratio. IL modified the optical properties as shown by the variation of band gap from 1.23 to 1.38 eV. Hollow $CoFe_2O_4$ microspheres were efficiently synthesized by Ni *et al.* [31] utilizing a solvothermal technique in the presence of a long-chain IL, [C_{18}mim]Br. Synthesized cubic spinel $CoFe_2O_4$ hollow spheres were characterized by a uniform size ranging from 100 to 200 nm in diameter and a shell thickness of around 10 to 50 nm. However, it is still unclear how cations and anions affect nucleation and growth behavior to change the morphology of $CoFe_2O_4$.

To the best of our knowledge, no prior study has been conducted on using 2 ILs with a common cation and atomically different (F or H) anions as templates to regulate morphology and correlate with structure and control optical and electrocatalytic properties. As a nanosynthetic template, we employed 1-ethyl-3-methylimidazolium trifluoromethanesulphonate ([C_2mim]CF_3SO_3) and 1-ethyl-3-methylimidazolium methanesulphonate ([C_2mim]CH_3SO_3) (**Figure 1**) to synthesize $CoFe_2O_4$ from iron(III) nitrate nonahydrate and cobalt(II) nitrate hexahydrate in a hydrothermal method. Our goal is to understand how anions play a major role in tuning the morphology of $CoFe_2O_4$. Thus, we utilized the unique supramolecular arrangement of 2 ILs having a common cation to control morphologies of $CoFe_2O_4$ NPs. To demonstrate the impact of controlled morphology on catalysis, we employed $CoFe_2O_4$ for OER under alkaline conditions. We showed how IL can effectively produce distinct morphologies to provide smaller spherical particles with an OER-active facet for performance enhancement. We also demonstrated the subtle variation of band gap with changing anion of ILs. This study provides a design principle for tuning nanostructure of $CoFe_2O_4$ using IL-assisted hydrothermal synthesis for optimizing optical and electrocatalytic properties.

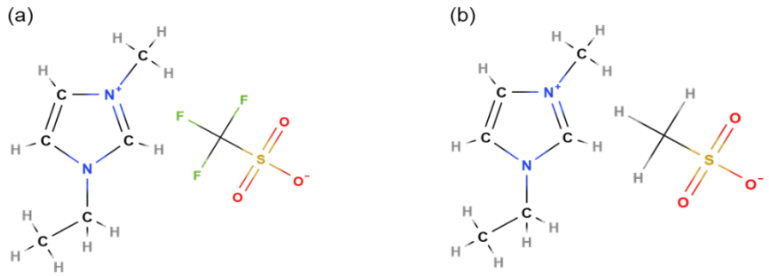

Figure 1 Structure of 2 ILs (a) 1-ethyl-3-methylimidazolium trifluoromethanesulphonate ([C_2mim]CF_3SO_3) and (b) 1-ethyl-3-methylimidazolium methanesulphonate ([C_2mim]CH_3SO_3) used to synthesize $CoFe_2O_4$ NPs.

Materials and methods

Materials

Iron(III) nitrate nonahydrate ($Fe(NO_3)_3.9H_2O$) (Sigma Aldrich) and cobalt nitrate hexahydrate ($Co(NO_3)_2.6H_2O$) (SMART-LAB) were used as precursors to synthesize $CoFe_2O_4$. 1-ethyl-3-methylimidazolium methanesulfonate [C_2mim]CH_3SO_3 (Fluka) and 1-ethyl-3-methylimidazolium trifluoromethanesulfonate [C_2mim]CF_3SO_3 (Sigma Aldrich) were used as templates. NaOH (Merck) and HCl (Sigma Aldrich) were employed to adjust the pH of the reaction medium. Deionized water and 30 wt% ethanol were used to separate and wash NPs. Nafion-117 solution (NANOCHEMAZONE), isopropanol (AnalaR), and carbon black acetylene (Alfa Aesar) were used with $CoFe_2O_4$ to prepare catalyst ink. 1.0 M KOH (Merck) was used as electrolyte for OER studies. All of the reagents were used without further purification.

Synthesis of $CoFe_2O_4$

$CoFe_2O_4$ was synthesized using $[C_2mim]CF_3SO_3$ and $[C_2mim]CH_3SO_3$ in a hydrothermal method. 8.5 mmol of IL was dissolved in 20 mL of water through vigorous stirring for 10 min. The 17 mmol of $Fe(NO_3)_3 \cdot 9H_2O$ and 8.5 mmol of $Co(NO_3)_2 \cdot 6H_2O$ were added under stirring. The pH of the mixture was adjusted to 11 with NaOH and HCl solutions, and volume was adjusted to 50 mL with DI water. It was sonicated for 15 min and transferred to a 75 mL Teflon container placed within a stainless-steel hydrothermal reactor. The mixture was treated hydrothermally at 150 °C for 20 h. The resulting product was washed with DI water and 30 wt% ethanol multiple times, then separated using an external magnet. The obtained product was dried at 80 °C for 2 h and then preserved in a vial under a tightly sealed environment. The identical procedure was followed for the synthesis of $CoFe_2O_4$ without the use of any IL. The schematic diagram in **Figure 2** illustrates the hydrothermal synthesis process of $CoFe_2O_4$.

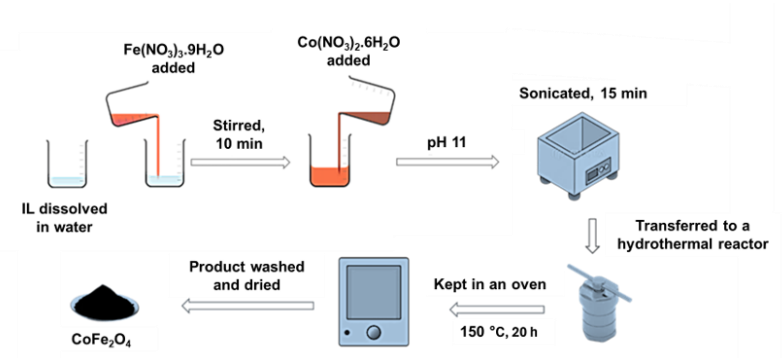

Figure 2 Schematic diagram for the hydrothermal synthesis of $CoFe_2O_4$ NPs.

Characterization

The obtained product was characterized by the Fourier transform infrared (FTIR) spectroscopic technique using KBr pellets (1:100 of $CoFe_2O_4$/KBr) with an FTIR-NIR spectrometer (Perkin Elmer, USA), ranging from 400 to 4,000 cm^{-1}. Elemental analysis was performed using energy-dispersive X-ray (EDX) spectroscopy (ZEISS Sigma 300, Germany, and Hitachi S3400N). The same instrument was employed for morphological analysis using field-emission scanning electron microscopy (FESEM) at an accelerating voltage of 5 kV. Hydrodynamic diameters of $CoFe_2O_4$ dispersed in DI water were estimated at a fixed angle of 90° and with a 632.8 nm He-Ne laser using a Zetasizer Nano ZS90 (ZEN90, Malvern Instruments Ltd., UK). Detailed crystal structure and phase purity were determined using a powder X-ray diffraction (PXRD) instrument (Ultima IV) with Cu Kα_1 radiation (0.15406 nm) and Bragg angles ranging from 10° to 70°. The generated patterns were compared with the ICDD 00-022-1086 pattern to confirm the FCC spinel structure of $CoFe_2O_4$. Diffuse reflectance spectra (DRS) were recorded from 200 to 800 nm using a PerkinElmer (LAMBDA 1050+) double-beam UV-Vis-NIR spectrophotometer, and the optical band gap was determined by the Kubelka-Munk (K-M) method.

Electrochemical measurements

Linear sweep voltammetry (LSV) was performed using CH Instruments (CHI 760E, USA) to evaluate the OER performance in alkaline (1.0 M KOH) conditions. A three-electrode cell consisting of a glassy carbon electrode (GCE) with a 3 mm diameter and an effective geometric surface area of 0.0707 cm^2 was employed as the working electrode (WE). A platinum counter electrode (CE) and an Ag/AgCl reference electrode (RE) were used. The catalyst ink was prepared by combining $CoFe_2O_4$ and carbon black acetylene in a 5:1 mass ratio, and isopropanol (IPA) and water in a 5:1 volume ratio, using Nafion-117 as the binder. The mixture was sonicated to achieve a homogeneous $CoFe_2O_4$ ink at 6.667 mg mL^{-1}. The GCE was polished with α-Al_2O_3 (initially 3 microns and followed by 0.05 microns) and sonicated for 30 min. The electrode was modified by drop-casting 15 µL (1 µL at a time) of ink onto the GCE to achieve a loading mass of 1.414 mg cm^{-2}. The electrodes were then dried overnight in a vacuum oven at 40 °C and 200 mbar. To obtain the LSV

polarization curve, a scan rate of 10 mV S^{-1} was used with iR drop correction. The pH of the solution was measured, and Eq. (1) was used to calculate the potential at a reversible hydrogen electrode (E_{RHE}). The overpotential was calculated based on Eq. (2), where 1.23 represents the thermodynamic potential for OER. The Tafel slope has been calculated using Eq. (3) from the LSV plot of the linear region to extract the kinetic mechanism.

$$E_{RHE} = E_{AgCl} + 0.059pH + 0.198 \quad (1)$$

$$\eta = E_{RHE} - 1.23\,V \quad (2)$$

$$\eta = a + b\,logj \quad (3)$$

Results and discussion

$CoFe_2O_4$ NPs were successfully synthesized in the hydrothermal method at 150 °C for 20 h to analyze the effect of $[C_2mim]CF_3SO_3$ and $[C_2mim]CH_3SO_3$ on the morphology. **Table 1** lists all synthesized materials, which have been labeled according to their use of IL. The samples were labeled as CFO-0, CFO-F, and CFO-M for CoFe2O4 without any IL (hence 0), in the presence of $[C_2mim]CH_3SO_3$ (M for methanesulfonate), and $[C_2mim]CF_3SO_3$ (F for trifluoromethanesulfonate), respectively.

Table 1 Nomenclature of $CoFe_2O_4$ synthesis from different reaction media.

Abbreviated Name	Ionic Liquid Used
CFO-0	No IL
CFO-F	8.5 mmol $[C_2mim]CF_3SO_3$
CF0-M	8.5 mmol $[C_2mim]CH_3SO_3$

Successful formation of $CoFe_2O_4$ NPs has been confirmed by analyzing FTIR and EDX spectra. To analyze the functional groups, FTIR spectra of $CoFe_2O_4$ NPs were obtained and are shown in **Figure 3**. Characteristics absorption due to lattice vibrations at the tetrahedral (A) and octahedral (B) sites of a spinel $CoFe_2O_4$ were used to identify the structure. All the synthesized $CoFe_2O_4$ NPs exhibited two characteristic absorption bands. An absorption band ~470 cm^{-1} confirms metal-oxygen (M-O) vibration at the B site. A sharp band ~580 cm^{-1} corresponds to the M-O vibration frequency at the A site. These two bands demonstrate the formation of a spinel structure. A broad absorption band around ~3,430 and ~1,630 cm^{-1} is due to the -OH stretching and bending frequencies, respectively. A higher vibrational frequency at the A site due to the lower reduced mass of M-O can arise from the substitution of Co by Fe. High-frequency shifts can also occur due to increased bond strength, leading to a higher effective nuclear charge, Z_{eff} or charge density.

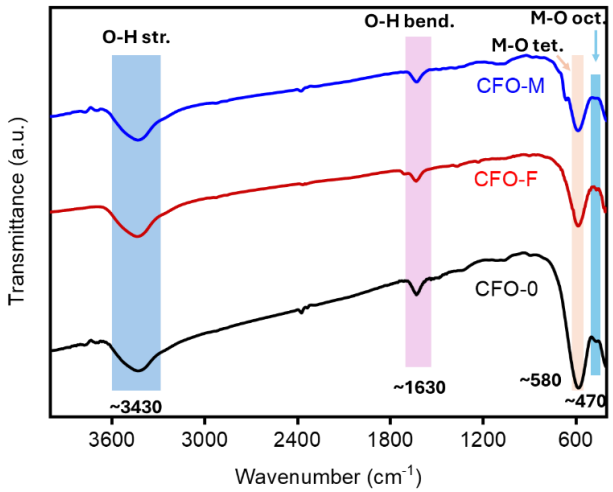

Figure 3 FTIR spectra of $CoFe_2O_4$ synthesized in two ILs and without IL, demonstrating vibrational frequencies of octahedral and tetrahedral sites.

As shown in **Table 2**, $CoFe_2O_4$ prepared in IL media exhibits an upshifted M-O(B) vibrational frequency in its FTIR spectrum. A large shift in vibrational frequency from 465 to 504 cm^{-1} at the B site was observed for CFO-F, which was synthesized in 8.5 mmol $[C_2mim]CF_3SO_3$. CFO-M, which was prepared using 8.5 mmol $[C_2mim]CH_3SO_3$, demonstrates a negligible change in vibrational frequency at the B site. A shift in vibrational frequency here indicates changes in cation occupancy. The resulting upshifting at the B site might be due to the large number of Fe^{3+} (lower reduced mass and larger Z_{eff}). Consequently, the displaced Co^{2+} occupies the A site. A strong interaction between neighboring M-O-M bonds could also increase the force constant and lead to an upshift in frequency. Meanwhile, this shows the ability of both ILs to modify the cationic distribution in lattice sites. The effect is more pronounced in the case of $[C_2mim]CF_3SO_3$, which has six hydrogen bond acceptor sites. Through strong hydrogen bonding with $Fe(OH)_4^-$, $[C_2mim]CF_3SO_3$ governs the distribution of Fe^{3+}. The effect is less prominent in $[C_2mim]CH_3SO_3$, which has only 3 hydrogen bond acceptor sites. ILs were successfully removed from the surface of the $CoFe_2O_4$, as there are no strong peaks around 1,030 cm^{-1}, which is responsible for $[C_2mim]^+$ cation, and 925 cm^{-1} (responsible for SO_3 in triflate-rich solution) [32].

Table 2 Vibrational frequencies of $CoFe_2O_4$ synthesized in $[C_2mim]CF_3SO_3$, $[C_2mim]CH_3SO_3$, and without IL.

Sample	ϑ M-O(B) (cm^{-1})	ϑ M-O(A) (cm^{-1})	ϑ_{OH} (bending) (cm^{-1})	ϑ_{OH} (stretching) (cm^{-1})
CFO-0	465	577	1,632	3,433
CFO-F	504	580	1,638	3,435
CFO-M	472	584	1,629	3,431

Elemental analysis using EDX spectra, as shown in **Figure 4**, further indicates the formation of the spinel structure of $CoFe_2O_4$. It possesses an elemental ratio of Co: Fe of nearly 1:2 in CFO-0, CFO-F, and CFO-M. Moreover, the Co, Fe, and O ratios were estimated around 1:2:4, which is in good agreement with the literature value of $CoFe_2O_4$.

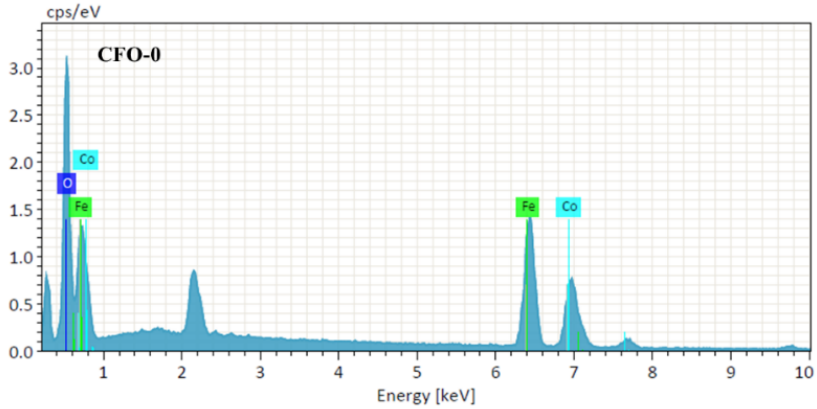

Figure 4 EDX spectrum of $CoFe_2O_4$ synthesized without IL.

To analyze the effect of ILs on the distribution of hydrodynamic diameter, DLS measurement of CoFe2O4 was performed using water as a dispersion medium at 25 °C. **Figure 5** shows that the highest hydrodynamic diameter (117 nm) was obtained for CFO-0. IL-assisted synthesis exhibits smaller hydrodynamic diameters. CFO-F shows an average hydrodynamic diameter of 96 nm, while that of CFO-M is 64 nm. Reduction in hydrodynamic diameter in presence of $[C_2mim]CF_3SO_3$ can be ascribed to the different environments. $[C_2mim]CF_3SO_3$ has a lower surface tension (39.2 mN m^{-1}) than water (72 mN m^{-1})

at room temperature, which allows a higher nucleation rate than the growth rate. Thus, smaller NPs are produced when $[C_2mim]CF_3SO_3$ has been used as a template. Compared to water, the higher viscosity (39.8 cP) of $[C_2mim]CF_3SO_3$ restricts the ion diffusion. This, in turn, leads to a smaller growth rate than the nucleation rate. Using six hydrogen bond acceptor sites, $[C_2mim]CF_3SO_3$ makes hydrogen bonds with the $Fe(OH)_4^-$ and $Co(OH)_3^-$ clusters to restrict their growth further. Steric hindrance provided by the $[C_2mim]CF_3SO_3$ could further affect the nucleation and growth of NPs. The physicochemical properties of $[C_2mim]CH_3SO_3$ are different from $[C_2mim]CF_3SO_3$, which mainly originate from the $CH_3SO_3^-$ anion. $[C_2mim]CH_3SO_3$ produces the smallest particle among the three cases due to the high viscosity of 135.0 cP, low surface tension of 41.3 mN m^{-1}, and low conductivity of 3.69 mS cm^{-1}. This slowed ion diffusion further, thereby restricting the growth of NPs.

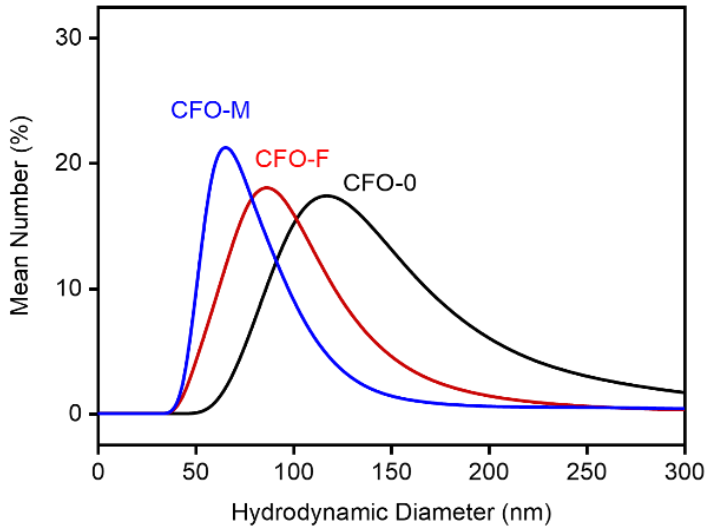

Figure 5 Hydrodynamic diameter distribution of $CoFe_2O_4$ synthesized without IL and with $[C_2mim]CF_3SO_3$ and $[C_2mim]CH_3SO_3$.

Different hydrodynamic diameters of NPs indicate distinct particle morphologies resulting from different growth patterns. Faster nucleation and slower growth rates are accountable for the formation of smaller NPs and vice versa. **Figure 6** shows FESEM images of three synthesized $CoFe_2O_4$ to analyze the morphology obtained under different reaction conditions. The one synthesized without IL exhibits a nanocube with a size of 84 nm. Uniform nanospheres were obtained for both CFO-F and CFO-M. However, the average size of the NPs obtained from $[C_2mim]CF_3SO_3$ is smaller than that obtained from $[C_2mim]CH_3SO_3$. Particles almost five times smaller than those obtained without using IL were formed from IL-based media due to growth restrictions. Also, uniform particles were produced in IL media to slow the growth of NPs. Synthesis without IL results in a cubic shape due to the preferential growth of one face over the others, driven by surface energy. The surface energy in various facets of the FCC crystal with lattice constant "a" follows: (110) > (100) > (111). In the beginning, growth rates of all low-index facets are similar. Later, the growth of the high-energy (110) facet decreases, and preferential growth in (100) and (111) facets leads to the formation of a nanocube [33].

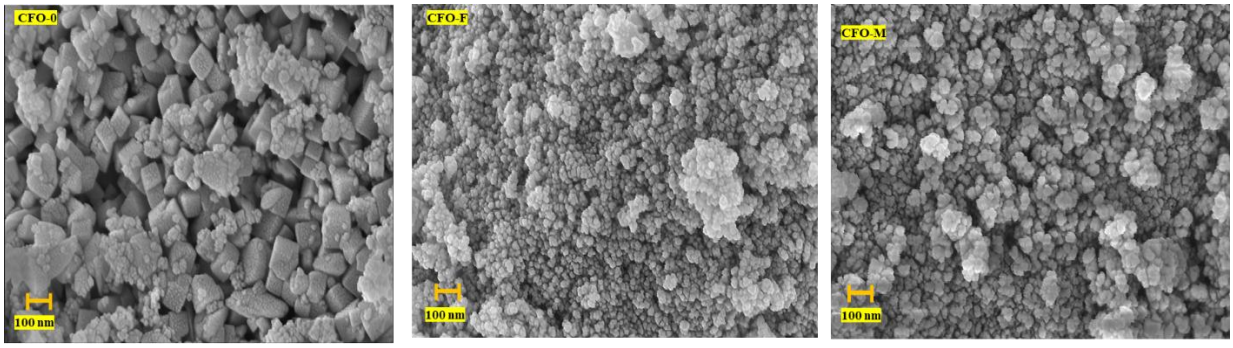

Figure 6 FESEM image of $CoFe_2O_4$ synthesized in different reaction media, such as without IL and with $[C_2mim]CF_3SO_3$ and $[C_2mim]CH_3SO_3$.

IL restricts particle growth before they reach this inhomogeneity in surface energy at various facets. Then, nuclei grow uniformly across all facets to decrease the overall interfacial free energy, thereby stabilizing the particles. ILs can adsorb at the particle surface via hydrogen bonding and van der Waals interactions. Moreover, the two ILs used here differ in hydrogen-bond-forming capacity and steric hindrance, which dictate particle size. It reveals that the cation of IL has a greater influence on particle shape, while the anion dictates particle size with a minor effect on shape. A schematic representation of the different shapes obtained with various ILs is shown in **Figure 7**. The morphological variation observed in the ILs is due to self-assembled structures formed by hydrogen bonding, electrostatic interactions, steric hindrance, and π-π stacking. The anions present in two ILs can selectively influence the growth process. Compared to $CH_3SO_3^-$, the higher hydrogen-forming $CF_3SO_3^-$ anion shows an enhanced effect in controlling the size of the particle.

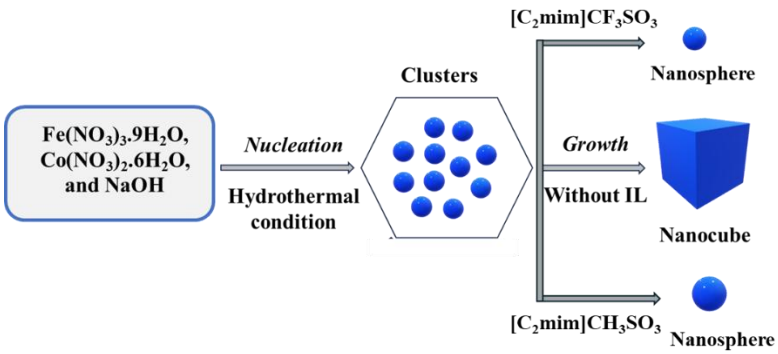

Figure 7 Schematic representation of various shapes obtained with the variation of the reaction media.

To diagnose the influence of ILs on the crystallite size, crystallinity, and phase purity of the $CoFe_2O_4$, in-depth PXRD analysis was performed. **Figure 8** displays the PXRD patterns of the $CoFe_2O_4$ nanomaterials. The sizes of the crystallites and percentage of crystallinity of the $CoFe_2O_4$ NPs resulting from the optimization process are listed in **Table 2**. The PXRD pattern shows good agreement with the cubic spinel $CoFe_2O_4$ (ICDD 00-022-1086), which possesses Bragg diffraction peaks (111) at 18.20°, (220) at 30.08°, (311) at 35.40°, (400) at 43.05°, (422) at 53.40°, (511) at 56.90°, and (440) at 62.50°. So, IL-assisted hydrothermal method was successful in preparing cubic spinel $CoFe_2O_4$. This indicates $CoFe_2O_4$ possesses an *Fd3m* space group. Nevertheless, the hydrothermal method without IL produced a less crystalline (92%) phase, including an impure hematite (ICDD 00-079-0007) phase. The corresponding peaks of hematite are (104) at 33.07°, (113) at 40.73°, and (024) at 49.47°. $CoFe_2O_4$ synthesized using $[C_2mim]CF_3SO_3$ possesses higher crystallinity (96%) compared to CFO-0, as shown in **Table 3**. While $CoFe_2O_4$ synthesized using $[C_2mim]CH_3SO_3$ also shows enhanced crystallinity (96%) with a smaller crystallite size. Highly crystalline

materials were obtained using ILs, which can be attributed to the orderly arrangement of ILs. It indicates that IL guides the packing of ions in the crystal, enabling the controlled synthesis of highly crystalline $CoFe_2O_4$ nanomaterials. The crystallite sizes of the synthesized materials were determined using the Debye-Scherrer formula at the (311) plane. Among 2 ILs, $[C_2mim]CH_3SO_3$ acts better than $[C_2mim]CF_3SO_3$ in attaining a smaller crystallite size. The distinct growth patterns in different reaction media control crystallite size and crystallinity.

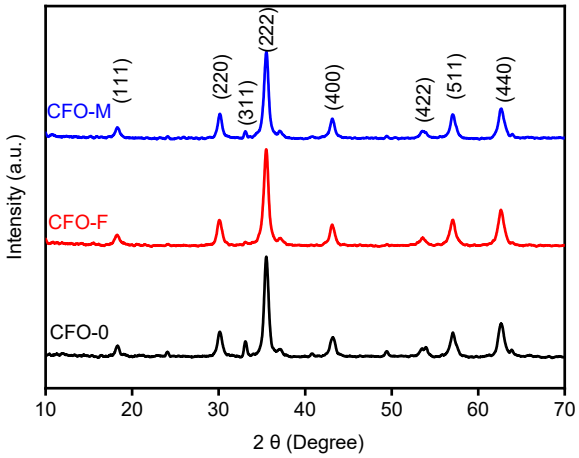

Figure 8 PXRD patterns of $CoFe_2O_4$ are synthesized in different reaction media, such as without IL and with $[C_2mim]CF_3SO_3$ and $[C_2mim]CH_3SO_3$.

Table 3 The degree of crystallinity and crystallite size for the $CoFe_2O_4$ are obtained from different reaction media.

Material	Crystallite Size (nm)	Crystallinity (%)
CFO-0	13	92
CFO-F	14	96
CFO-M	11	96

Figure 9 shows the Tauc plot of $CoFe_2O_4$ with its corresponding band gaps at different synthesis conditions. CFO-0 exhibits the highest band gap energy of 1.93 eV. At the same time, CFO-F and CFO-M exhibit a smaller band gap. With the increase of Co^{2+} ions in the A site, alternatively with the increase of Fe^{3+} at the B site, the band gap energy is reduced [30]. The FTIR data also suggest similar changes, with a large positive shift in the vibration frequency of M-O(*oh*) attributed to the increased number of Fe^{3+} ions at the B site. Crystal structure, morphology, defects, and distribution of cations across A and B sites influence the nanoscale optical properties of $CoFe_2O_4$. Here, *d-d* transitions of metal cations and charge transfer are mainly responsible for the optical band gap of $CoFe_2O_4$. The crystal field generated by O^{2-} causes the *d* orbitals of metal cations to split into the e_g and t_{2g} levels. It is important to note that the energy width is larger for B sites than for A sites. The relationship between the energy differences at the A site and the B site is as follows:

$$\nabla_t = \frac{4}{9} \nabla_O \quad (4)$$

The distribution of Co^{2+} ions between the A and B sites in the spinel structure of $CoFe_2O_4$ alters the optical band gap due to the difference in HOMO to LUMO gap, intersublattice charge transfer, intervalence charge transfer, and Z_{eff} at octahedral and tetrahedral sites. Hence, the fluctuation in the band gap of $CoFe_2O_4$ NPs can be attributed to the non-equilibrium distribution of Fe^{3+} and Co^{2+} ions in both A and B sites, which is influenced by different morphologies of $CoFe_2O_4$ NPs

[10]. Moreover, a defective site created by ILs alters the band gap by introducing intermediate energy levels [34].

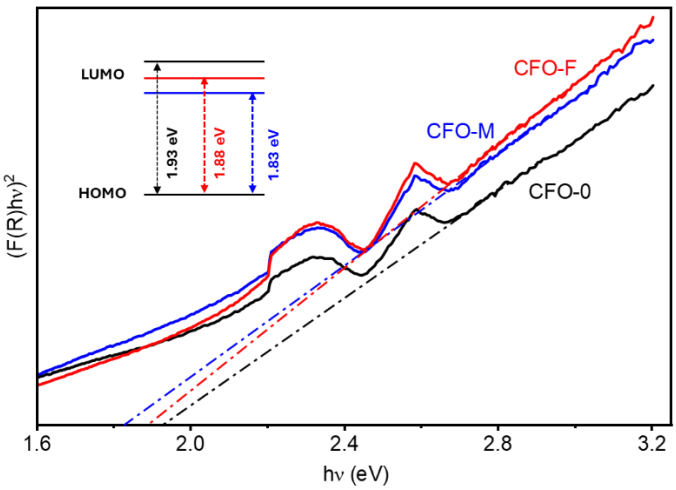

Figure 9 Tauc plots of $CoFe_2O_4$ are synthesized in different reaction media, including without IL (black) and with $[C_2mim]CF_3SO_3$ (red) and $[C_2mim]CH_3SO_3$ (blue).

Absorption spectra of $CoFe_2O_4$ have the superposition of *d-d* transition and charge transfer processes. Therefore, $CoFe_2O_4$ possesses two band gaps (indirect band gap below 2.0 eV and direct band gap above 2.0 eV). Similar behavior has been reported by Holinsworth *et al.* [35]. Further, Dileep *et al.* [36] also demonstrated both indirect and direct band gaps around ~1.5 and 2.3 eV, respectively, using high-resolution electron energy loss spectroscopy [36]. The lower-energy indirect transition is associated with the intersublattice charge transfer (~1.75 eV) and crystal field transition (~1.9 eV) of tetrahedrally coordinated Co^{2+} ions [37]. This also indicates the normal spinel structure where Co^{2+} occupies the tetrahedral site. Here, $CH_3SO_3^-$ is more effective in reducing the band gap of $CoFe_2O_4$ (from 1.93 to 1.83 eV) than CF_3SO_3. This clearly demonstrates the impact of ILs on the redistribution of cations to alter the band gap. So, the intrinsic electronic properties of CFO-M are different from those of CFO-F. This behavior impacts their resulting electrocatalytic properties.

LSV measurements were taken to evaluate the electrocatalytic properties towards OER. The LSV curves of $CoFe_2O_4$ synthesized using $[C_2mim]CF_3SO_3$ are shown in **Figure 10**. While CFO-0 requires a large onset overpotential of 362 mV, CFO-M requires only a small onset overpotential of 303 mV. CFO-F also demonstrated a lower onset overpotential than CFO-0. A similar trend is observed in the overpotential required to achieve a current density of 10 mA cm^{-2}. The improved OER activity of CFO-M is due to its smaller particle size and higher surface area, which provide more active sites than CFO-0. Moreover, OER activities depend on the exposed facet of the nanomaterial along with the energy required to bind the intermediates (OH^* and OOH^*). For the ferrite-type materials, OER favors at the (111) facet over the (001) or (100) facet, as demonstrated by Davis *et al.* [19] Spherical particles have more exposed (111) facets compared to the cubic shape [38]. Compared to a flat cubic surface, spherical nanoparticles have inherently higher active sites due to low-coordination surface atoms. Uncoordinated or low-coordinated Co^{2+} or Fe^{3+} are widely recognized as OER active sites [39]. CFO-M and CFO-F have a nano-spherical morphology, showing improved current density. This indicates that the morphology of the exposed crystal facet directly affects electrocatalytic activity. Moreover, CFO-M has a smaller optical band gap; it should possess a higher electrical conductivity due to high charge carrier mobility, which in turn reduces the overpotential. Enhanced OER activity of CFO-M is also related to the large number of Fe^{3+} at the B site, as evidenced by the band gap and FTIR data. Further analysis of the Tafel plot provides insight into the kinetics at different surfaces.

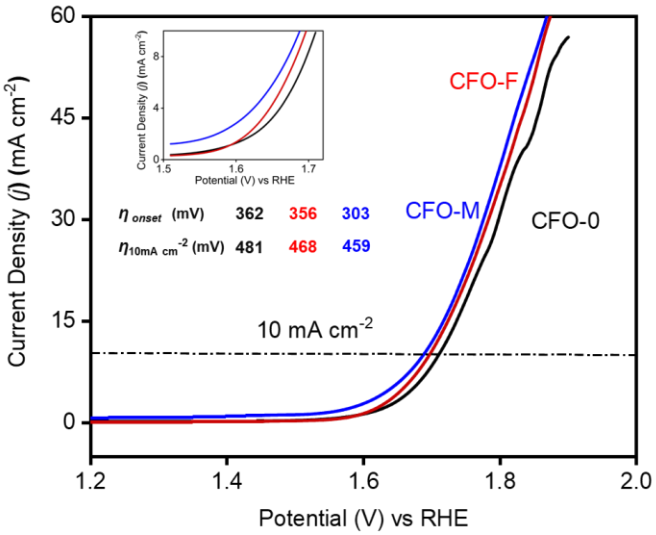

Figure 10 LSV polarization curves (scan rate = 10 mV s^{-1}) of $CoFe_2O_4$ synthesized in different reaction media, including without IL and with $[C_2mim]CF_3SO_3$ and $[C_2mim]CH_3SO_3$. The inset represents the zoomed-in LSV curve around the onset potential.

CFO-F exhibits the smallest Tafel slope of 103 mV dec^{-1} compared to both CFO-M (185 mV dec^{-1}) and CFO-0 (122 mV dec^{-1}), as shown in **Figure 11**. Having the smallest particle size, CFO-F has a large open surface and active sites; therefore, it has faster kinetics. As CFO-F has been synthesized from IL having $CF_3SO_3^-$, the electronic structure and Co^{2+}/Fe^{3+} distribution might be altered by the electron-withdrawing F atom. Thus, faster kinetics might originate from a subtle change in the d-band center and adsorption energies of OER intermediates (OH* and OOH*) due to the electronic effects of F atoms on the $CoFe_2O_4$ [40]. Although the kinetics per active site are faster, CFO-F requires a higher onset overpotential (356 mV) due to particle aggregation driven by the high surface energy of smaller particles.

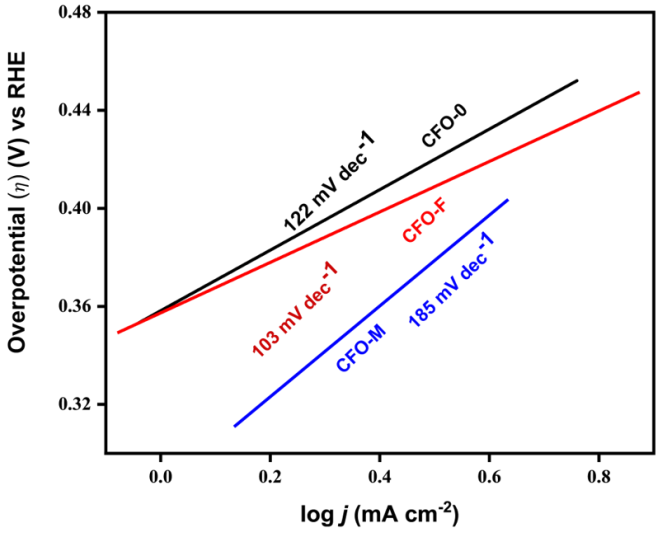

Figure 11 Tafel slope derived from LSV plots at a scan rate =10 mV s^{-1} in 1.0 M KOH for $CoFe_2O_4$ synthesized without IL (black) and with $[C_2mim]CF_3SO_3$(red) and $[C_2mim]CH_3SO_3$ (blue).

On the other hand, CFO-M demonstrates sluggish kinetics, although it has the lowest onset overpotential and overpotential to achieve 10 mA cm^{-2}. The higher current density and lowest onset overpotential can be explained by unaggregated nanospheres that have low-coordinated active sites and exposed (111) facets. But the high Tafel slope value of 185 mV dec^{-1} indicates that O-O Bond formation is kinetically hindered due to the stronger binding of intermediates with the surface of NPs. The largest Tafel slope of CFO-M might also originate from the heterogeneous and broad distribution of Co^{2+}/Fe^{3+}; therefore, multiple steps are involved, which limit the reaction kinetics. Also, CFO-M contains a small amount of hematite impurity, which can alter the local active site distribution. Beyond the catalytic activity, the stability of $CoFe_2O_4$ under alkaline OER conditions makes it a robust catalyst. Guo *et al.* [41] reported the stability of $CoFe_2O_4$ at 50 mA cm^{-2} current density for 100 h using chronopotentiometric measurement in 1.0 M KOH. Negligible content of Co and Fe was found in the electrolyte using inductively coupled plasma optical emission spectroscopy (ICP-OES), which indicates $CoFe_2O_4$ remains stable under operational conditions. Through a multistep chronopotentiometric measurement, a long-term stability of $CoFe_2O_4$ for 100 h was demonstrated by Lee *et al.* [42]. Exceptional durability for 100 h at high current density (500 mA cm^{-2}) was reported by Shen *et al.* [43]. Tunable OER activity and long-term stability of $CoFe_2O_4$ make it a suitable candidate for real-world applications. Importantly, ILs allow modifying morphology to control the low-coordinated active sites and exposed facets for improvement of OER performance.

This study demonstrates the role of 2 imidazolium-based ILs in controlling morphologies through distinct preferential interactions of $CH_3SO_3^-$ and $CF_3SO_3^-$ to produce 5 times smaller nanospherical particles from the nanocube. IL acts as a structure-directing template, as the crystal produced from IL is free from hematite impurity. Both hydrophilic ILs were removed from the surface without further degradation of the structure of the nanoparticles. ILs alter the cationic distribution and optical properties as evidenced by the change in band gaps associated with the Co^{2+} occupancies in lattice sites. This indicates that tunable electronic properties of $CoFe_2O_4$ could be achieved using IL as soft templates. IL produced smaller spherical particles that have a high surface area and low-coordinated active sites for OER. Moreover, spherical particles have predominantly (111) exposed facet that enhances the OER activity. Thus, the electrocatalytic and optical properties of $CoFe_2O_4$ can be tuned by controlling crystal structure and morphology using ILs as guiding templates. Further research can be conducted to evaluate the effect of IL concentration on morphology and electrocatalytic properties. Keeping the same anion, different cations of IL can be chosen to prepare $CoFe_2O_4$ to see their impact on morphology. A systematic variation of physicochemical properties of ILs and their correlation with morphology and catalytic activities will provide deeper mechanistic insight into designing ferrite-type materials. Quantitative analysis of cations in tetrahedral and octahedral sites will provide in-depth insights into improved OER performance and tunable optical properties. Further analysis on the modification of the magnetic properties of $CoFe_2O_4$ with cationic distribution using ILs will provide a new method to control magnetic properties, which may help to understand the spin effect on OER.

Conclusions

The synthesis of $CoFe_2O_4$ magnetic nanoparticles from iron(III) nitrate nonahydrate and cobalt(II) nitrate hexahydrate using $[C_2mim]CF_3SO_3$ and $[C_2mim]CH_3SO_3$ in a hydrothermal method was successful. Ionic liquids function as soft templates, enabling precise control over the size and shape of the synthesized $CoFe_2O_4$ materials. Both ILs modified the morphology from cubic to spherical, with 5 times smaller particles (17 nm) than the native ones (84 nm). Phase pure and highly crystalline FCC spinel form of $CoFe_2O_4$ was achieved by employing $[C_2mim]CH_3SO_3$. $[C_2mim]CF_3SO_3$ exhibited greater interaction with Fe^{3+} due to its F atom in anion, allowing for control over its distribution between tetrahedral and octahedral sites. IL reduces the optical band gap energy of $CoFe_2O_4$ from 1.93 to 1.83 eV via modifying cationic distribution, changing *d-d* transition, and intersublattice charge transfer. $CoFe_2O_4$ synthesized using 8.5 mmol of $[C_2mim]CH_3SO_3$ exhibited improved activity in the oxygen evolution reaction (OER), which is

demonstrated by a low onset overpotential of only 303 mV as well as a low overpotential of 459 mV to achieve 10 mA cm^{-2}. This has been ascribed to the large number of active sites, the high surface area of the smaller nanoparticles, and the exposed (111) facet. However, faster kinetics (103 mV dec^{-1}) was observed for the $CoFe_2O_4$ synthesized using 8.5 mmol of $[C_2mim]CF_3SO_3$. This might arise from the change in local electronic environment and low-coordinated active sites produced by a fluorine-dominated anion. This demonstrates the ability of ILs to tune the structure of $CoFe_2O_4$ to produce optimized nanostructures and electronic properties that enhance OER activity. Therefore, IL can be used to control the morphology of any ferrite-type materials for tunable band gaps and desired exposed facets.

An in-depth analysis of the nucleation and growth mechanisms of NPs will provide further insight into the reported absence of hematite impurities in the presence of ILs. Systematic variation of physicochemical properties of ILs to tune the morphology of $CoFe_2O_4$ can be performed to illustrate their effects. The cooperative effect of 2 ILs can be observed by the formation of double salt ionic liquids with different molar ratios of individual ionic liquids. Quantitative analysis of the distribution of cations between octahedral and tetrahedral sites in $CoFe_2O_4$ synthesized with ILs will provide strong support behind the observed improvement in OER performance and change in optical properties. The OER activity of the $CoFe_2O_4$ magnetic NPs may further be enhanced by applying an external magnetic field. Research to address these issues is now underway.

Acknowledgements

The authors gratefully acknowledge UGC Research Grant 2024-2025 from University Grants Commission of Bangladesh for Dhaka University teachers for a Research Project.

Declaration of generative AI in scientific writing

Generative artificial intelligence (GenAI) was not used in this work. We, the author, take full responsibility for the content, claims, and references.

CRediT author statement

Md Hasibul Hasan: Conceptualization, Methodology, Investigation, Data Curation, Writing - Original Draft Preparation, Formal Analysis. **Md. Abu Bin Hasan Susan**: Conceptualization, Supervision, Resources, Funding acquisition, Project Administration, Reviewing and Editing.

References

[1] C Acar and I Dincer. The potential role of hydrogen as a sustainable transportation fuel to combat global warming. *International Journal of Hydrogen Energy* 2020; **45(5)**, 3396-3406.

[2] A Odenweller and F Ueckerdt. The green hydrogen ambition and implementation gap. *Nature Energy* 2025; **10(1)**, 110-123.

[3] H Tüysüz. Alkaline water electrolysis for green hydrogen production. *Accounts of Chemical Research* 2024; **57(4)**, 558-567.

[4] Y Lee, J Suntivich, KJ May, EE Perry and Y Shao-Horn. Synthesis and activities of rutile IrO_2 and RuO_2 nanoparticles for oxygen evolution in acid and alkaline solutions. *The Journal of Physical Chemistry Letters* 2012; **3(3)**, 399-404.

[5] L Royer, A Bonnefont, T Asset, B Rotonnelli, JJ Velasco-Vélez, S Holdcroft, S Hettler, R Arenal, B Pichon and E Savinova. Cooperative redox transitions drive electrocatalysis of the oxygen evolution reaction on cobalt–iron core–shell nanoparticles. *ACS Catalysis* 2023; **13(1)**, 280-286.

[6] ON Avcı, L Sementa and A Fortunelli. Mechanisms of the oxygen evolution reaction on $NiFe_2O_4$ and $CoFe_2O_4$ inverse-spinel oxides. *ACS Catalysis* 2022; **12(15)**, 9058-9073.

[7] T Li, Y Lv, J Su, Y Wang, Q Yang, Y Zhang, J Zhou, L Xu, D Sun an Y Tang. Anchoring $CoFe_2O_4$ nanoparticles on N-doped carbon nanofibers for high-performance oxygen evolution reaction. *Advanced Science* 2017; **4(11)**, 1700226.

[8] S Choudhary, A Bisht and S Mohapatra. Facile synthesis, morphological, structural, photocatalytic and optical properties of $CoFe_2O_4$ nanostructures. *SN Applied Sciences* 2019; **48(22)**, 34033-34045.

[9] R Rai, S Wilser, M Guminiak, B Cai and M Nakarmi. Optical and electronic properties of

$NiFe_2O_4$ and $CoFe_2O_4$ thin films. *Applied Physics A* 2012; **106(1)**, 207-211.

[10] Y Kumar, A Sharma and PM Shirage. Impact of different morphologies of $CoFe_2O_4$ nanoparticles for tuning of structural, optical and magnetic properties. *Journal of Alloys and Compounds* 2019; **778**, 398-409.

[11] K Kombaiah, JJ Vijaya, LJ Kennedy, M Bououdina, RJ Ramalingam and HA Al-Lohedan. Comparative investigation on the structural, morphological, optical, and magnetic properties of $CoFe_2O_4$ nanoparticles. *Ceramics International* 2017; **43(10)**, 7682-7689.

[12] Y Sugawara, K Kamata, A Ishikawa, Y Tateyama and T Yamaguchi. Efficient oxygen evolution electrocatalysis on $CaFe_2O_4$ and its reaction mechanism. *ACS Applied Energy Materials* 2021; **4(4)**, 3057-3066.

[13] P Thakur, N Gahlawat, P Punia, S Kharbanda, B Ravelo and A Thakur. Cobalt nanoferrites: A review on synthesis, characterization, and applications. *Journal of Superconductivity and Novel Magnetism* 2022; **35(10)**, 2639-2669.

[14] W Bian, Z Yang, P Strasser and R Yang. A $CoFe_2O_4$/graphene nanohybrid as an efficient bi-functional electrocatalyst for oxygen reduction and oxygen evolution. *Journal of Power Sources* 2014; **250**, 196-203.

[15] P Li, R Ma, Y Zhou, Y Chen, Q Liu, G Peng, Z Liang and J Wang. Spinel nickel ferrite nanoparticles strongly cross-linked with multiwalled carbon nanotubes as a bi-efficient electrocatalyst for oxygen reduction and oxygen evolution. *RSC Advances* 2015; **5(90)**, 73834-73841.

[16] Z Zhang, AJ Rondinone, J-X Ma, J Shen and S Dai. Morphologically templated growth of aligned spinel $CoFe_2O_4$ nanorods. *Advanced Materials* 2005; **17(11)**, 1415-1419.

[17] S Jha, P Jain, R Palkovits and PP Ingole. Tuning of cationic distribution in "partially inverted" cobalt ferrite spinel nanocubes via a nitrogen-doped graphene oxide support for enhanced bifunctional oxygen electrocatalysis. *Journal of Materials Chemistry A* 2023; **11(42)**, 23034-23047.

[18] S Rafiezadeh, A Chaitram and R Pentcheva. Cooperative effect of Co and Fe promotes the OER activity of $CoFe_2O_4$ (100) and (001) surfaces. *ChemCatChem* 2026; **18(1)**, e01290.

[19] EM Davis, A Bergmann, H Kuhlenbeck and B Roldan Cuenya. Facet dependence of the oxygen evolution reaction on Co_3O_4, $CoFe_2O_4$, and Fe_3O_4 epitaxial film electrocatalysts. *Journal of the American Chemical Society* 2024; **146(20)**, 13770-13782.

[20] SM Ansari, BB Sinha, D Phase, D Sen, PU Sastry, YD Kolekar and CV Ramana. Particle size, morphology, and chemical composition controlled $CoFe_2O_4$ nanoparticles with tunable magnetic properties via oleic acid-based solvothermal synthesis for application in electronic devices. *ACS Applied Nano Materials* 2019; **2(4)**, 1828-1843.

[21] S Rafiezadeh, V Begum-Hudde and R Pentcheva. Electronic and optical properties of the fully and partially inverse $CoFe_2O_4$ spinel from first principles calculations including many-body effects. *Physical Review B* 2024; **109(19)**, 195172.

[22] JP Singh, JY Park, V Singh, SH Kim, WC Lim, H Kumar, YH Kim, S Lee and KH Chae. Correlating the size and cation inversion factor in context of magnetic and optical behavior of $CoFe_2O_4$ nanoparticles. *RSC Advances* 2020; **10(36)**, 21259-21269.

[23] MP Reddy, AMA Mohamed, XB Zhou, S Du and Q Huang. A facile hydrothermal synthesis, characterization and magnetic properties of mesoporous $CoFe_2O_4$ nanospheres. *Journal of Magnetism and Magnetic Materials* 2015; **388**, 40-44.

[24] RM Cheriyan, I Anila and MJ Mathew. Characterization and magnetic phase resolution of $CoFe_2O_4$ nanocubes and nanospheres. *AIP Conference Proceedings* 2019; **2162(1)**, 020098.

[25] NM Refat, MY Nassar and SA Sadeek. A controllable one-pot hydrothermal synthesis of spherical cobalt ferrite nanoparticles: Synthesis, characterization, and optical properties. *RSC Advances* 2022; **12(38)**, 25081-25095.

[26] AL Lopes-Moriyama, V Madigou, CP De Souza and C Leroux. Controlled synthesis of $CoFe_2O_4$ nano-octahedra. *Powder Technology* 2014; **256**, 482-489.

[27] G Ji, S Tang, S Ren, F Zhang, B Gu and Y Du. Simplified synthesis of single-crystalline magnetic

$CoFe_2O_4$ nanorods by a surfactant-assisted hydrothermal process. *Journal of Crystal Growth* 2004; **270(1-2)**, 156-161.

[28] Y Huang, W Yang, Y Yu and S Hao. Ordered mesoporous spinel $CoFe_2O_4$ as an efficient electrocatalyst for the oxygen evolution reaction. *Journal of Electroanalytical Chemistry* 2019; **840**, 409-414.

[29] AS Shahvelayati and A Tanha. A review of ionic liquids: From solvent applications to template-assisted synthesis of metal oxide nanoparticles. *Applied Organometallic Chemistry* 2025; **39(4)**, e70026.

[30] A Ghaemi, F Mohave, A Farhadi, MA Takassi and H Tavakkoli. Hydrothermal synthesis of mesoporous cobalt ferrite by ionic liquid-assisted process; catalytic performance, morphology, and magnetic studies. *Journal of the Australian Ceramic Society* 2021; **57(4)**, 1321-1330.

[31] X Ni, Z He, X Liu, Q Jiao, H Li, C Feng and Y Zhao. Ionic liquid-assisted solvothermal synthesis of hollow $CoFe_2O_4$ microspheres and their absorbing performances. *Materials Letters* 2017; **193**, 232-235.

[32] CM Burba, NM Rocher and R Frech. Hydrogen-bonding and ion-ion interactions in solutions of triflic acid and 1-ethyl-3-methylimidazolium triflate. *The Journal of Physical Chemistry B* 2009; **113(33)**, 11453-11458.

[33] HG Liao, D Zherebetskyy, H Xin, C Czarnik, P Ercius, H Elmlund, M Pan, LW Wang and H Zheng. Facet development during platinum nanocube growth. *Science* 2014; **345(6199)**, 916-919.

[34] A Pancielejko, M Kroczewska-Gnatowska, P Mazierski, J Łuczak and A Zaleska-Medynska. The effect of ionic liquids on the surface and photocatalytic properties of semiconducting materials. *Chemical Engineering Journal* 2024; **498**, 155274.

[35] BS Holinsworth, D Mazumdar, H Sims, QC Sun, MK Yurtisigi, SK Sarker, A Gupta, WH Butler and JL Musfeldt. Chemical tuning of the optical band gap in spinel ferrites: $CoFe_2O_4$ vs $NiFe_2O_4$. *Applied Physics Letters* 2011; **98(26)**, 261917.

[36] K Dileep, B Loukya, N Pachauri, A Gupta and R Datta. Probing optical band gaps at the nanoscale in $NiFe_2O_4$ and $CoFe_2O_4$ epitaxial films by high-resolution electron energy loss spectroscopy. *Journal of Applied Physics* 2014; **116(10),** 103505.

[37] L Kampermann, J Klein, J Korte, O Kowollik, O Pfingsten, T Smola, S Saddeler, TH Piotrowiak, S Salamon, J Landers, H Wende, A Ludwig, S Schulz and G Bacher. Link between structural and optical properties of $Co_xFe_{3-x}O_4$ nanoparticles and thin films with different Co/Fe ratios. *The Journal of Physical Chemistry C* 2021; **125(26)**, 14356-14365.

[38] Z Liu, HM Amin, Y Peng, M Corva, R Pentcheva and Tschulik. Facet-dependent intrinsic activity of single Co_3O_4 nanoparticles for oxygen evolution reaction. *Advanced Functional Materials* 2023; **33(1)**, 2210945.

[39] MS Burke, S Zou, LJ Enman, JE Kellon, CA Gabor, E Pledger and SW Boettcher. Revised oxygen evolution reaction activity trends for first-row transition-metal (oxy) hydroxides in alkaline media. *The Journal of Physical Chemistry Letters* 2015; **6(18)**, 3737-3742.

[40] J Qian, Q Shu, B He, Y Hua, X Ge, D Sun, W Liu, Q Zhang and L Zhou. Fluorine decoration induced deep reconstruction of iron cobalt oxide for high-efficiency oxygen evolution reaction. *International Journal of Hydrogen Energy* 2024; **68**, 777-787.

[41] FY Guo, J Luan, XC Meng, P Zheng, WL Duan and WZ Li. Optimization of conductivity and stability on inverse spinel $CoFe_2O_4$ for alkaline oxygen evolution reaction. *Chemical Engineering Journal* 2025; **523**, 168363.

[42] G Lee, M Jeong, HR Kim, M Kwon, S Baek, S Oh, M Lee, D Lee and JH Joo. Controlled electrophoretic deposition strategy of binder-free $CoFe_2O_4$ nanoparticles as an enhanced electrocatalyst for the oxygen evolution reaction. *ACS Applied Materials & Interfaces* 2022; **14(43)**, 48598-48608.

[43] H Shen, H Du, P Li and M Wang. Hierarchical flaky spinel structure with Al and Mn co-doping towards preferable oxygen evolution performance. *Materials* 2025; **18(15)**, 3633.